THESIS ON CIVIL ENGINEERING F9

APPLICATION OF SATELLITE DATA FOR MONITORING THE MARINE ENVIRONMENT

LIIS SIPELGAS

Faculty of Civil Engineering
Department of Environmental Engineering
TALLINN UNIVERSITY OF TECNOLOGY

Dissertation was accepted for the commencement of the degree of Doctor of Philosophy in Natural Sciences on March 23, 2006

Supervisor: Ph.D Urmas Raudsepp, Marine Systems Institute at TUT

Opponents: Ph.D Priit Tisler, Finnish Meteorological Institute

Ph.D Tiit Kutser, Estonian Marine Institute,
University of Tartu

Commencement: June 2nd, 2006

Declaration: Hereby I declare that this doctoral thesis, my original investigation and achievement, submitted for the doctoral degree at Tallinn University of Technology has not been submitted for any degree or examination.

Liis Sipelgas

ISSN 1406-4766
ISBN 9985-59-616-1

Contents

List of Publications

This thesis is based on the following papers, which will be referred to in the text by their Roman numerals.

I. *Sipelgas, L.*, Arst, H., Raudsepp, U., Kõuts, T., Lindfors, A. 2004. Optical properties of coastal waters of northwestern Estonia: in situ measurements. Boreal Environment Research, 5(9), 447–459.

II. *Sipelgas, L.*, Raudsepp, U., Kõuts, T. 2006. Operational monitoring of suspended matter distribution using MODIS images and numerical modelling. Advanced Space Research, accepted for publication.

III. Leppäranta, M., Reinart, A., Erm, A., Arst, H., Hussainov, M., *Sipelgas, L.* 2003. Investigation of ice and water properties and under-ice light field in fresh and beackish water bodies. Nordic Hydrology, 34(3), 245–266.

IV. Arst, H., *Sipelgas, L.* 2004. In situ and satellite observations of optical properties of the ice cover in the Baltic Sea region, Proceedings of the Estonian Academy of Sciences Biology, Ecology., 53(1) 25–36.

1 Introduction

Optical remote sensing has become one of the main methods of aquatic environment research and monitoring, as a tool involving techniques and methods for gathering operative information over large areas. Thus it is becoming a cheaper tool than traditional *in situ* measurements. Environmental remote sensing is generally considered as having begun with the launch of Landsat on board ERTS-1 in 1972. The Coastal Zone Color Scanner (CZCS) on board the Nimbus satellite launched in 1978 was the first optical instrument designed especially for the remote sensing of the oceans. The CZCS was replaced by Sea-viewing Wide Field-of-view Sensor (SeaWiFS) on board the SeaStar in 1997 and later by Moderate Resolution Imaging Spectroradiometer (MODIS) on board the satellites Terra and Aqua in 2000 and 2001 and MEdium Resolution Imaging Spectrometer (MERIS) on board ENVISAT in 2002.

The basic principles of determining water quality parameters from remote sensing data rely on the conventional theory of light transfer (Gordon, 1975; Kirk, 1994; Mobley, 1994). The characteristics of light are greatly affected by the nature of the aquatic medium when it passes it. Solar radiation penetrating water diminishes with depth due to a change in the energy spectrum as a result of absorption and scattering caused by water and its constituencies. As known, eutrophication may significantly change the amount and spectral composition of solar radiation penetrating a water body. Thus the optical characteristics of the natural water and underwater radiation field may be considered as indicators of the ecological state of the water body.

The coastal sea is the primary receiver of particles, nutrients and dissolved organics from rivers and other land-based sources. Also an anthropogenic impact affects the water quality in the coastal sea. As a result, the water transparency decreases, which sustains eutrophication. Eventually, natural and anthropogenic loads onto the coastal sea may result in sharp gradients of biogeochemical parameters between the coastal and the open sea. Optical research methods for coastal sea and inland water studies have received increasing attention in recent years (Dekker, 1993; Kutser, 1997; Reinart, 2000; Herlevi, 2002), where satellite remote sensing could be an important tool.

This dissertation discusses:

- Inherent optical properties of water and ice, and their relations to optically active substances.
- Application of remote sensing data for water quality monitoring during strong anthropogenic impact caused by harbour dredging.
- Application of remote sensing data for ice cover monitoring.

2 Theory

Kirk (1994) gave thorough explanations and definitions of essential physical parameters that characterize properly the light field in a water. Below I briefly summarize the definitions of these parameters.

Radiant flux (Φ, W) is the time rate of flow of radiant energy.

Radiant intensity at a point in space (I, $\mathrm{Wsr^{-1}}$) is the radiant flux at that point in a specified direction in an infinitesimal cone containing the given direction, divided by that element of solid angle, $d\omega$,

$$I = \frac{d\Phi}{d\omega}. \tag{1}$$

Irradiance (E, $\mathrm{Wm^{-2}}$) is the radiant flux per unit area of a surface, dS,

$$E = \frac{d\Phi}{dS}. \tag{2}$$

Surface radiance as a function of direction ($L(\theta,\phi)$, $\mathrm{Wm^{-2}sr^{-1}}$) is the radiant flux emitted in a given direction per unit solid angle per unit projected area of a surface

$$L(\theta,\phi) = \frac{d^2\Phi}{dS\cos\theta d\omega} \equiv \frac{dE}{\cos\theta d\omega}, \tag{3}$$

where θ is the zenith angle and ϕ is the azimuth angle.

Using the surface radiance the total downward irradiance (E_d, $\mathrm{Wm^{-2}}$) at a point in that surface can be obtained by integrating the surface radiance with respect to the solid angle over the whole upper hemisphere

$$E_d = \int_{2\pi} L(\theta,\phi)\cos\theta d\omega. \tag{4}$$

The total upward irradiance (E_u, $\mathrm{Wm^{-2}}$) is defined similarly

$$E_u = -\int_{-2\pi} L(\theta,\phi)\cos\theta d\omega,$$

where θ is between 90º and 180º.

The net downward irradiance ($\vec{E}$, $\mathrm{Wm^{-2}}$) is

$$\vec{E} = E_d - E_u = \int_{4\pi} L(\theta,\phi)\cos\theta d\omega. \tag{5}$$

The scalar irradiance (E_0, $\mathrm{Wm^{-2}}$) is the integral of the radiance distribution at a point over all directions around the point

$$E_0 = \int_{4\pi} L(\theta,\phi)d\omega. \tag{6}$$

The downward scalar irradiance (E_{0d}, $\mathrm{Wm^{-2}}$) is the integral of the radiance distribution over the upper hemisphere

$$E_{0d} = \int_{2\pi} L(\theta,\phi)d\omega, \tag{7}$$

and the upward scalar irradiance (E_{0u}, Wm^{-2}) is the integral of the radiance distribution over the lower hemisphere

$$E_{0u} = \int_{2\pi} L(\theta,\phi)d\omega. \tag{8}$$

Radiation fields vary considerably with wavelength across the photosynthetically active region.

The propagation of light in the water–atmosphere system is governed by the integral differential equation of radiative transfer, which contains absorption and scattering parameters that are characteristic of the particular water body under investigation. Unfortunately these parameters can not yet be measured with sufficient accuracy to allow the derivation of the inwater light field with the Radiative Transfer Equation (RTE).

2.1 Inherent optical properties

The inherent optical properties (IOP) depend only on the type and concentration of substances present in the medium. There are two main processes, absorption and elastic scattering, quantified by the absorption coefficient and the volume scattering function, respectively, that control the manner in which impinging photons propagate through an aquatic medium. Their definition is based on a small volume with thickness Δr, illuminated by a narrow collimated beam of monochromatic light of spectral radiant power ϕ_i, Figure 1. The absorption coefficient (a, m^{-1}) is defined as the limit of the fraction absorbed power when Δr goes to zero (Mobley, 1994):

$$a \equiv \lim_{\Delta r \to 0} \frac{\phi_a}{\phi_i \Delta r}. \tag{9}$$

The volume scattering function (β, sr^{-1},m^{-1}) is defined as the limit of the fraction scattered light when both Δr and $\Delta\Omega$ go to zero (Mobley, 1994):

$$\beta(\psi) \equiv \lim_{\Delta r \to 0} \lim_{\Delta\Omega \to 0} \frac{\phi_s(\psi)}{\phi_i \Delta r \Delta\Omega}. \tag{10}$$

Integrating β over all scattering angles we get the scattering coefficient (b, m^{-1}) (Mobley, 1994):

$$b \equiv 2\pi \int_0^{\pi} \beta(\psi)\sin\psi d\psi. \tag{11}$$

The total scattering coefficient is the sum of forward scattering coefficient (b_f, m^{-1}) and backward scattering coefficient (b_b, m^{-1}) (or simply backscattering coefficient). These coefficients can be defined as follows (Kirk, 1994):

$$b_f \equiv 2\pi \int_0^{\pi/2} \beta(\psi)\sin\psi d\psi \,, \tag{12}$$

$$b_b \equiv 2\pi \int_{\pi/2}^{\pi} \beta(\psi)\sin\psi d\psi \,, \tag{13}$$

The beam attenuation coefficient (c, m^{-1}) is defined as the sum of absorption and scattering coefficient (Mobley, 1994):

$$c = a + b \,. \tag{14}$$

The absorption and scattering coefficients are functions of wavelength, in other words the IOP have spectral dependence.

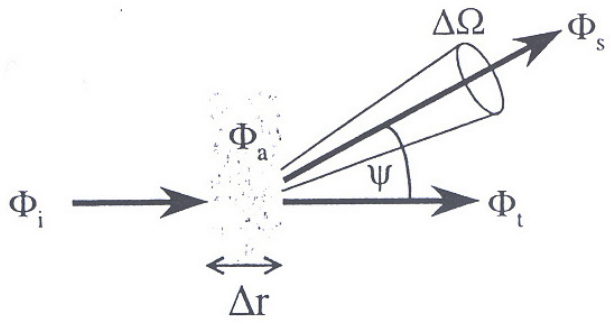

Figure 1. The definitions of inherent optical properties are based on a collimated beam illuminating an infinitesimal layer (from Mobley, 1994).

2.2 Apparent optical properties

Apparent optical properties (AOP) depend both on the medium and on the ambient light field. However, they display sufficiently regular features and stability to be useful descriptors of the water body.

Diffuse attenuation coefficient of downwelling light, K_d, m^{-1}, and subsurface irradiance reflectance, $R(0–)$, are commonly used AOP as they are sensitive to changing water compositions and often behave well with depth.

In a vertically homogeneous water body the values of all spectral irradiances diminish in an approximately exponential manner with depth. Hence, we can specify its logarithmic change rate and this will be about the same at all depths. We define the vertical attenuation coefficient for downward irradiance as:

$$K_d \equiv -\frac{1}{E_d}\frac{dE_d}{dz} \,. \tag{15}$$

An important AOP, which provides information about the angular structure of light field, is the subsurface irradiance reflectance:

$$R(0-) \equiv \frac{E_u(z=0)}{E_d(z=0)}. \tag{16}$$

The most used optical property of sea ice is the albedo. The spectral albedo is simply defined as the fraction incident irradiance that is reflected from the ice surface:

$$\alpha(\lambda) = \frac{E_u(0,\lambda)}{E_d(0,\lambda)}, \tag{17}$$

where E_u is the upwelling irradiance at wavelength λ, E_d is the downwelling irradiance at wavelength λ and 0 designates the surface. Wavelength integrated, or total, albedo is often a quantity of interest, since it is the measure of the total solar energy absorbed in the water body (Maykut and Untersteiner, 1971; Maykut and Petrovich, 1987). It is expressed as follows:

$$\alpha_t = \frac{\int \alpha(\lambda) E_d(0,\lambda) d\lambda}{\int E_d(0,\lambda) d\lambda}. \tag{18}$$

The total albedo depends on the spectral distribution of the incident irradiance as well as on the spectral albedo of the surface. Thus a change in cloud conditions, and thereby in the incident spectral irradiance, can result in changes in the total albedo (Grenfell and Maykut, 1977).

3 Introduction to optics of natural waters

The incident solar radiation field that reaches the Earth's surface consists of a direct beam component from the Sun and a diffuse component from the clouds and atmospheric particles. The interaction of light with the water column is shown on Figure 2. The main processes that incident light will undergo while penetrating into the water are scattering and absorption, some portion of the light is also reflected from the surface. The relative portions of these processes are dependent on the physical properties of the water column and on the wavelength of the light.

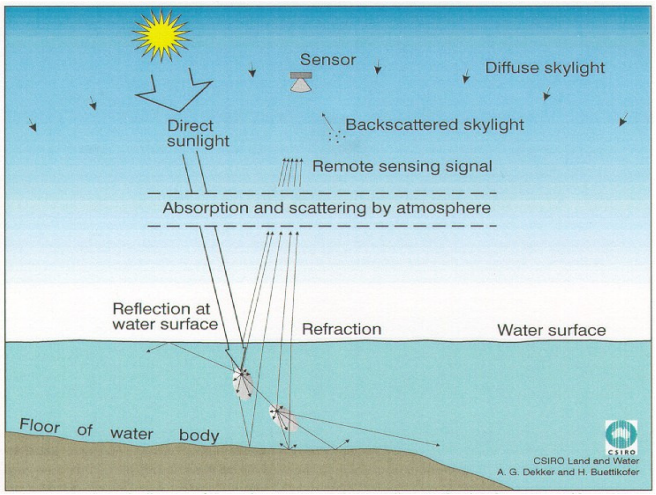

Figure 2. Interaction of light with the water column.

The interaction of solar radiation with ice cover is illustrated schematically in Figure 3. Depending on sky and surface conditions some portion of the incident radiation is reflected from the surface, some is reflected form the ice, a portion is absorbed and scattered in the ice, and a portion is transmitted through the ice. The relative sizes of these portions are dependent on physical properties of the ice and on the wavelength of the light.

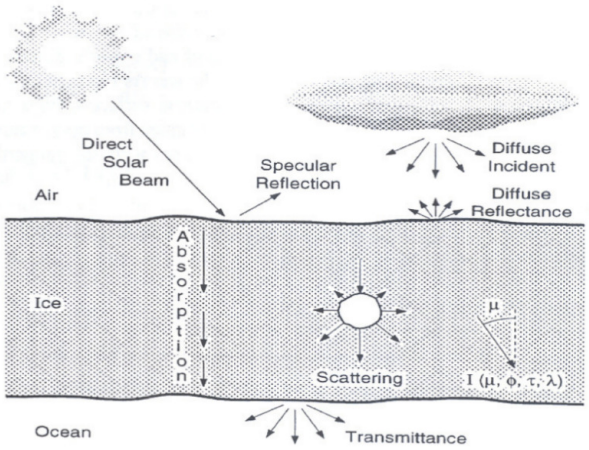

Figure 3. Scheme of radiative transfer in the sea ice (from Petrovich, 1994).

Thus far, the radiative transfer equation has defied analytical solution forcing one to resort to numerical methods i.e. model simulations. There are a number of mathematical methods for solving the RTE numerically (Gordon et al. 1975; Kirk, 1981; Mobley, 1994).

In bio-optics the commonly used solution was developed by Gordon et al. (1975). In their Monte-Carlo study they were able to fit irradiance reflectance just beneath the water surface with the polynomial function of absorption and backscattering coefficients, which can be simplified to:

$$R(\lambda,0-)=C\frac{b_b(\lambda)}{a(\lambda)+b_b(\lambda)}, \tag{19}$$

where $b_b(\lambda)$ is the total spectral backscattering coefficient, $a(\lambda)$ is the total spectral absorption coefficient and the value of C depends on the solar zenith angle (for the sun at the zenith C=0.32) (Gordon et al., 1975). It is obvious that an expression like equation (16) contains assumptions regarding the light field and the average shape of the volume scattering function. Using different computer modelling procedures, Prieur (1976) arrived at the same relationship, with C having the value 0.33. Further Monte-Carlo studies (Kirk, 1984) found the coefficient C to be a function of solar altitude, and it is reasonably well expressed as a linear function of μ_0, the cosine of the zenith angle of the refracted photons:

$$C_{\mu_0}=-0.629\mu_0+0.975\,. \tag{20}$$

From equations (19) and (20) follows that the irradiance reflectance just below the water surface can be calculated as follows:

$$R(\lambda,0-)=(0.629\mu_0+0.975)\frac{b_b(\lambda)}{a(\lambda)+b_b(\lambda)}. \tag{21}$$

3.1 Absorption and scattering in water

Pure water itself and optically active constituents of water (phytoplankton pigments, nonliving organic and mineral particles, and coloured dissolved organic matter) are the main contributors to the absorption and scattering process in the water column.

The spectral absorption coefficient of pure water (Figure 4) has been measured in several studies (Tyler and Smith, 1970; Smith and Baker, 1981; Pope and Fry, 1997) and is taken as known although there are some differences between the pure water absorption coefficient values taken from different studies. The scattering of pure water increases towards shorter wavelengths, while absorption decreases (Figure 4).

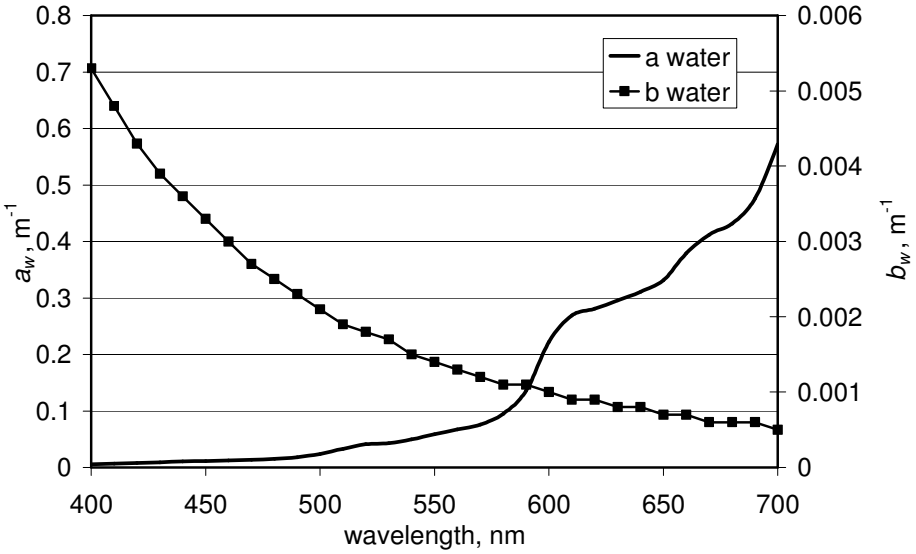

Figure 4. The spectra of absorption (a_w) and scattering (b_w) coefficients of pure water (Pope and Fry, 1997).

The origin of coloured dissolved organic matter (CDOM) is leaching from soil or decomposition of phytoplankton in the water body. CDOM consists of different chemical compounds. Despite its complex nature the spectral absorption coefficient of CDOM, $a_{CDOM}(\lambda)$, generally has an exponential shape and can be expressed by the following formula (Højerslev, 1980):

$$a_{CDOM}(\lambda) = a_{CDOM}(380)\exp(-S_{CDOM}(\lambda - 380)), \qquad (22)$$

where $a_{CDOM}(380)$ is the absorption coefficient of CDOM at 380 nm and S_{CDOM} is the slope factor. An example of $a_{CDOM}(\lambda)$ is shown in Figure 5. It is generally assumed that scattering by CDOM is negligible.

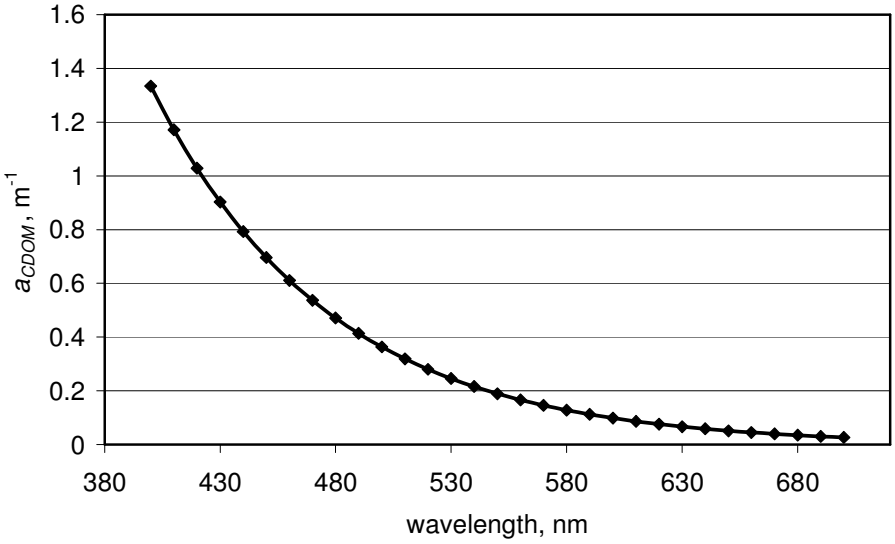

Figure 5. An example of the spectral absorption coefficient of CDOM (a_{CDOM}).

Absorption of phytoplankton (a_{ph}) is caused by their various pigment (clorophylls, carotenoids, biliproteins) composition, which can vary between different types of algae. Typically the absorption spectrum of phytoplankton has a maximum in the blue part of the spectrum (430–500 nm) and a secondary absorption peak in the red part (650–680 nm) of the spectrum.

Chlorophyll *a* occurs in all photosynthetic plants and often its concentration is used as a measure of phytoplankton abundance. To describe optical properties of different phytoplankton species or assemblages we can define chlorophyll-specific spectral absorption coefficient of phytoplankton, $a^*_{ph}(\lambda)$, as the absorption coefficient per unit of chlorophyll ($a^*_{ph}(\lambda) = a_{ph}(\lambda)/C_{chl}$). The values of $a^*_{ph}(\lambda)$ presented in the literature vary greatly. Dekker (1993) found that at 676 nm the a^*_{ph} varied from 0.0055 to 0.028 m^2 mg C_{chl}^{-1} in mesotrophic to eutrophic lakes in Holland. The general tendency also shows that $a^*_{ph}(\lambda)$ decreases when C_{chl} increases. Bricaud et al. (1995) found that the chlorophyll-specific spectral absorption coefficient of phytoplankton can be calculated using a power function:

$$a^*_{ph}(\lambda) = A(\lambda) C_{chl}^{-B(\lambda)}, \tag{23}$$

where $A(\lambda)$ and $B(\lambda)$ are positive, wavelength dependent parameters. The result was obtained for a variety of marine waters where the concentration of chlorophyll *a* was 0.02–25 μm/L. An example of $a^*_{ph}(\lambda)$ calculated according to equation (20) is shown in Figure 6.

Bricaud et al. (1983) investigated the scattering properties of phytoplankton. They concluded that the scattering is clearly depressed at the wavelengths where absorption is high. Kirk (1994) listed values of the chlorophyll-specific

scattering coefficient of phytoplankton, $b^*_{ph}(\lambda)$,($b^*_{ph}(\lambda) = b_{ph}(\lambda)/C_{chl}$), for different phytoplankton types ranging from 0.044 to 0.535 m^2 mg C_{chl}^{-1} at 550 or 590 nm. An example of $b^*_{ph}(\lambda)$ form data of Holland lakes published by Dekker (1993) is shown on Figure 6.

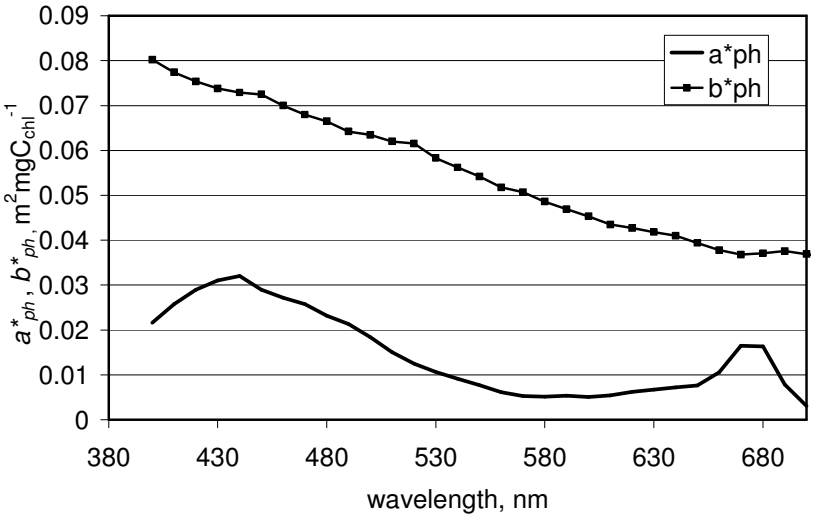

Figure 6. Chlorophyll-specific spectral absorption coefficient of phytoplankton (a^*_{ph}) calculated by equation (23), and spectral chlorophyll-specific scattering of phytoplankton (b^*_{ph}) taken from Dekker, 1993.

Nonliving organic particles are produced for example as phytoplankton die or zooplankton graze. Mineral particles in water can be sand, clay and metal oxides. Their mean absorption curves are of exponential shape with varying slopes. The absorption coefficient spectra increase towards shorter wavelengths (Bricaud and Stramski, 1990; Dekker, 1993). Examples of the particle-specific spectral absorption coefficient, $a^*_t(\lambda)$, ($a^*_t(\lambda) = a_t(\lambda)/C_t$) published in Ahn (1990) are presented in Figure 7.

Nonliving organic particles together with mineral particles, i.e. tripton, are the main light scatterers in water, especially the mineral particles. Scattering depends not only on the particle concentration, but also on their shape and internal structure, the index of refraction and the size distribution (Kirk, 1994; Jerlov, 1968). Examples of the particle-specific spectral scattering coefficients, $b^*_t(\lambda)$, ($b^*_t(\lambda) = b_t(\lambda)/C_t$) of two types of particles published by Ahn (1990) are presented in Figure 7.

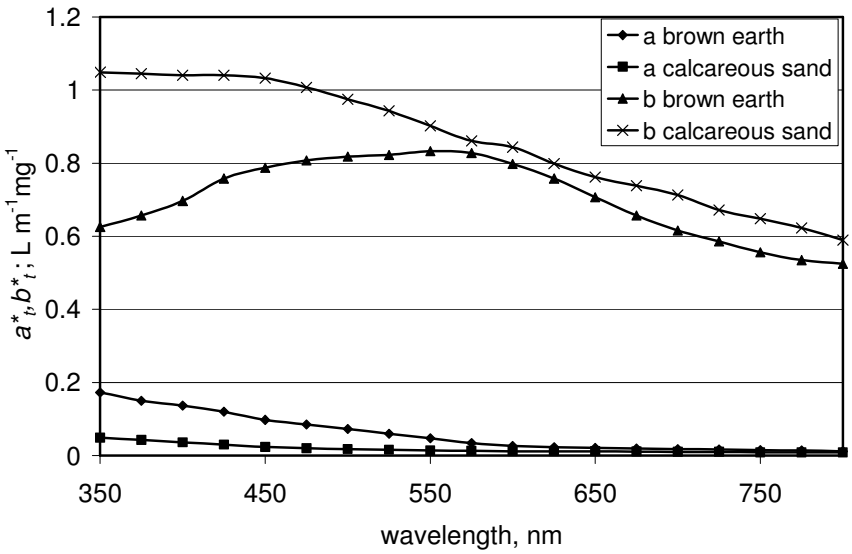

Figure 7. An example of particle-specific spectral absorption coefficient (a^*_t) and particle-specific spectral scattering coefficients (b^*_t) of brown earth and calcareous sand (Ahn, 1990).

The total spectral absorption coefficient, $a(\lambda)$, is the sum of absorption coefficients of optically active water constituents. If we assume that optically active components in water are CDOM, phytoplankton pigments and tripton together with pure water then the total absorption can be calculated as follows:

$$a(\lambda) = a_w(\lambda) + a^*_{ph}(\lambda)C_{chl} + a_{CDOM}(\lambda) + a^*_t(\lambda)C_t, \quad (24)$$

The total spectral scattering coefficient, $b(\lambda)$, is the sum of scattering coefficients of optically active water constituents. As mentioned before CDOM does not contribute to scattering. The total scattering coefficient is the sum of scattering coefficients of phytoplankton pigments, tripton and pure water:

$$b(\lambda) = b_w(\lambda) + b^*_{ph}(\lambda)C_{chl} + b^*_t(\lambda)C_t. \quad (25)$$

The total spectral backscattering coefficient, $b_b(\lambda)$, is needed for bio–optical modelling equation (16). The formula describing the backscattering is:

$$b_b(\lambda) = 0.5b_w(\lambda) + b^*_{bph}(\lambda)C_{chl} + b^*_{bt}(\lambda)C_t, \quad (26)$$

where $b^*_{bph}(\lambda)$ is the chlorophyll-specific spectral backscattering coefficient of phytoplankton and $b^*_{bt}(\lambda)$ is the particle-specific spectral backscattering coefficient of tripton. The coefficient 0.5 describes the backscattered fraction of the total scattering of pure water.

3.2 Absorption and scattering in the ice cover

The absorption in the sea ice is a sum of the absorption coefficients of ice, brine and air. The absorption coefficient of air in the sea ice is assumed to be zero. The spectral absorption coefficient for pure bubble free fresh ice has a strong wavelength dependence. The minimum absorption is in the blue part of the spectrum and the absorption is increasing with increasing wavelength. The absorption coefficient of brine is the sum of absorption coefficients of impurities e.g. particulates, sediments, ice biota, and CDOM. Absorption coefficients of these impurities vary depending on their optical properties and composition. The OAS in water, described in the previous section, can all be found in brine. In general these impurities are strongly absorbing and weekly scattering (Pertovich, 1994).

Scattering in sea ice results form differences in the real indices of refraction between ice and the inclusions (e.g. air bubbles, brine pockets). The greater the difference between the indices of refraction, the greater the scattering. The refraction index for ice is 1.31, the average refraction index for air bubbles is 1.0, but the index of refraction for brine depends on the temperature, increasing from 1.34 at –2 °C to 1.40 at –32 °C (Maykut and Light, 1995). So, the air bubbles are more strongly scattering than brine pockets. Higher number of inclusions in the sea ice increase the amount of scattering. However, the scattering coefficient depends not only on the amount of brine and air, but also on how these are distributed (Petrovich, 1994). According to several authors (Grenfell, 1983;1991; Petrovich, 1993) the scattering coefficients and scattering phase functions for sea ice can be assumed to be independent of wavelength.

3.3 Physical properties of ice

The physical properties of ice surface affect significantly the value of albedo. Albedos of different ice types have different absolute values and also wavelength dependence. In general albedo decreases as the surface changes from snow covered thick ice to young grey ice. Some examples from the literature are shown in Figure 8.

The sensitivity of albedo to thickness during the initial stages of ice growth was investigated by Weller (1972). His measurements showed a rapid rise in albedo from 0.08 to 0.40 as the ice grew from open water to a thickness of 0.30 m, followed by a more gradual asymptotic increase as the ice continued to grow. In addition to surface conditions also the internal state and structure of the ice can affect albedo. Both the volume and distribution of brine pockets and air bubbles affect the ice albedo (Petrovich, 1994). Petrovich (1994) and Grenfell (1981) found in laboratory experiments that increasing brine volume decreases albedo.

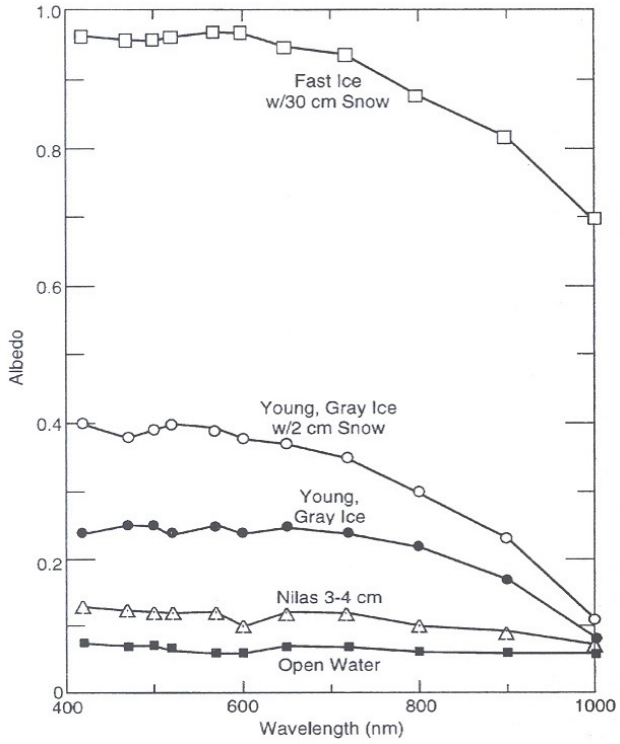

Figure 8. Spectral albedos of Antarctic sea ice (from Allison et al., 1993).

Light transmission through the ice cover is characterized by the transmittance $T(\lambda)$, that is the fraction of the incident irradiance that is transmitted through the ice. Light attenuation in the ice is often represented using an irradiance extinction coefficient $K(z,\lambda)$, which is defined similarly to ice free water by equation (15).

The magnitude and spectral distribution of light transmitted through the ice cover depends on the physical composition of the ice, its thickness and the surface conditions of the ice. The transmission decreases exponentially with the increasing ice thickness. The influence of the ice surface layer on transmittance was studied by Maykut and Grenfell (1975). They found that even a thin snow cover (0.25m) reduces light transmission through the ice to less than 1%. Ice biota also reduces the light transmission and changes its spectral composition (Maykut and Grenfell, 1975; Soo Ho et al., 1987; Petrovich et al., 1993).

4 Data and measurement methods
4.1 Study sites and data

Ice free period

The study region covers Estonian coastal sea from Pakri Bay to the Moonsund archipelago (Figure 1 in Paper I). Case study of Pakri Bay was performed under strong anthropogenic impact (dredging activities) while measurements in coastal waters were performed in natural conditions.

Field measurements in coastal waters of northwestern Estonian were carried out from 29 July to 2 August 2002. The study region includes archipelago (Moonsund) and coastal sea (northwestern coast of Estonia) areas, thus comprising the transition zone between two different types of water masses. Moonsund is influenced by river inflow that discharges nutrients, organic and inorganic suspended material and dissolved organic substances into the sea. The particular location of the coastal sea belongs to the area of strong hydrodynamic and biological variability (Suursaar et al., 1995; Pavelson et al., 1999).

A case study of the influence of harbour dredging on the optical properties of water was performed in Pakri Bay in 2002–2003 when Paldiski South harbour was intensively dredged.

The measurement programme included:

1. Laboratory measurements of the concentrations of chlorophyll *a* (C_{chl}, in μg/L), suspended matter and spectrofotometric beam attenuation coefficient of filtered (c^*, m^{-1}) and unfiltered water (c^*_f, m^{-1}) samples;
2. Continuous in situ measurements of light attenuation (c, m^{-1}) and absorption coefficients (a, m^{-1}) along the ship route by a flow through system based on WetLabs AC–9 instrument.

Ice-cover period

The fieldwork was performed in the winters of 2000–2003 in nine Estonian and Finnish lakes and in one brackish water site, Santala Bay, in the Gulf of Finland. General limnological data about the lakes are given in Table 1 of Paper IV.

The measurement programme included:

1. Snow and ice thickness;
2. Structure of ice samples based on thick and thin sections;
3. Laboratory measurements of the concentration of chlorophyll *a* (C_{chl}, in μg/L); the spectrophotometric beam attenuation coefficient of filtered (c^*, m^{-1}) and unfiltered water (c^*_f, m^{-1}) from melted ice samples (in some cases separately for different ice layers);
4. Albedo (A) of the ice (or snow) surface.
5. Averaged vertical attenuation coefficient of light ($K_{d,i}$) in the ice cover.
6. Transmittance (T) – the ratio of irradiance just under the ice cover to the value of incident irradiance.

4.2 Methods

4.2.1 Laboratory analyses

Laboratory analysis of concentrations of ***chlorophyll a***, ***suspended matter***, ***dissolved organic matter*** and the ***spectrometric attenuation coefficient*** were performed in the laboratory of the Marine systems Institute at TUT. A detailed description of the analysis methods and instrumentation used is given in Paper I

4.2.2 In situ measurements

Inherent optical properties of water, the light attenuation (c, m^{-1}) and absorption coefficients (a, m^{-1}) were measured using a flow through system based on an AC–9 instrument (attenuation and absorption meter manufactured by WetLabs Inc. USA). The description of the flow through system and instrumentation used is given in Lindfors and Rasmus (2000).

Radiation measurements were performed using a special instrument constructed for under ice measurements of the light field. The system was based on two different radiation sensors LI–192 SA and LI–193 SA (*LI–COR*, Inc., USA). The first sensor is for measurements of plane irradiance and the second sensor for scalar irradiance in the PAR band. A detailed description of the measurement system is given in Paper III

4.2.3 Satellite data

MODIS (or Moderate Resolution Imaging Spectroradiometer) is a key instrument aboard the Terra (EOS AM) and Aqua (EOS PM) satellites. The Terra's orbit around the Earth is timed so that it passes from the north to the south across the equator in the morning, while the Aqua passes from the south to the north over the equator in the afternoon. MODIS has 36 spectral bands ranging in wavelength from 400 to 14400 nm. The spatial resolution is 250 meters for the channels 1 and 2, 500 m for the channels 3–7 and 1000 m for the channels 8–36. The temporal coverage of the satellites where MODIS is installed enables us to receive 2–4 images per day. For analysis cloud free images were downloaded from GES Distributed Active Archive Center (http://daac.gsfc.nasa.gov/data/datapool/). For image processing the ENVI (The Remote Sensing Exploitation Platform, http://www.rsinc.com/envi/) software was used. Images were geocorrected and converted into reflectance values by using calibration coefficients (added to each MODIS image).

Image analysis during the ice free period

Reflectance data from MODIS bands in the visible wavelength range provide information on qualitative distribution pattern of OAS in the water. As mentioned in the previous section, MODIS has several bands with 1000 m

resolution in the visible range of the wave spectrum, but for studying the coastal areas a finer resolution is essential. Therefore MODIS bans 1 and 2 with spatial resolution of 250 m were used. In theory these bands are meant for atmospheric studies and should not have any contribution of water constituents. However, recent studies by Miller et al. (2004) and Hu et al. (2004) showed that these bands can also be used for estimating the concentration of suspended matter in optically complex coastal waters.

To get quantitative measure of the concentrations of suspended matter in the water surface the linear relationship between the remote sensing reflectance, R, at MODIS band 1 and the suspended matter concentration was obtained:

C_{SPM}, was $C_{SPM}=110.3\ R+2.0$ with $r^2=0.58$. (27)

Applying the equation (27) maps of spatial distribution of the concentration of suspended matter were obtained. Detailed information of used data is given in paper II.

Image analysis during the ice cover period

For the investigation of the spatial distribution of ice cover microwave instruments are usually applied. However, for measuring the spectral reflectance of the surface (needed for distinguishing different ice types and for analysis of energy exchange between the ocean and the atmosphere) multispectral radiometers are preferable (Riggs et al., 1999).

Global ice products with 1000 m resolution are produced by National Snow and Ice Data Centre (NSIDC). The standard algorithm is based on Normalized Difference Snow Index (NDSI) modified for sea ice to distinguish it from the open water, relying on reflective and thermal characteristics. All products are archived at the NSIDC in Boulder, Colorado. In these products "cloud mask" technique was used to eliminate the influence of clouds. However, Hall et al. (2002) showed that the "cloud mask" technique (Ackerman et al., 1998) as it is used currently in the MODIS standard products tends to overestimate the cloud cover. Thus, MODIS colour composite image gives a more realistic description of ice cover (Hall et al., 2002). Therefore, for analysing the ice cover distribution in the Gulf of Riga, Baltic Sea, we used MODIS data from channel 1 instead of the standard sea ice cover product. Ice reflectance is higher than water reflectance and therefore, sea ice was distinguished from the open water relying on the reflectance value at band 1 using the "Decision tree" tool in ENVI. A reflectance value less than 0.005 was considered to be indicate open water. All pixels that classified as ice were counted and the total ice extent in the Gulf of Riga in square kilometres was obtained for each classified image.

5. Results and Discussion

5.1 Relationships between inherent optical properties (IOP) and optically active substances (OAS) in coastal waters of northwestern Estonia (Detailed treatment in Paper I)

Relationships between IOP properties to concentrations of OAS are important for different applications. From the point of view of bio-optical modelling these relationships are needed for interpretation of remote sensing data. Also, in the in situ measurement systems IOP at some waveband are used for calculating the concentration of some OAS.

The spectral absorption and scattering coefficients together with concentrations of OAS were collected during the field study in coastal waters of northwestern Estonia in July 2002.

In data analysis correlations between the spectral absorption and scattering coefficients measured by AC–9, and concentrations of CDOM, chlorophyll *a* and suspended matter were studied.

The spectral absorption coefficient of CDOM is described by the exponential law, equation (22). Therefore the amount of CDOM is characterized by the light absorption coefficient at shorter wavelengths (370–420 nm). As Baltic waters have a relatively high concentration of CDOM compared to oceanic waters, CDOM has strong effect on the absorption properties (Højerslev and Aas, 2001; Kowalczuk, 1999). According to our dataset the linear regression between the absorption coefficient at 412 nm and the CDOM concentration was:

$$a(412) = 0.4288 C_{CDOM} + 0.1603 \qquad (28)$$

with the correlation coefficient $R = 0.94$.

As the absorption of CDOM is negligible at longer wavelengths (i.e. 650–750 nm), some authors (Claustre et al., 2000; McKee et al., 2003) found a linear correlation between the absorption at 676 nm and the chlorophyll *a* content in water. However, our data did not confirm this relationship (the correlation coefficient between these parameters was only 0.18). This may be due to the particle absorption influencing the absorption coefficient at 676 nm.

Scattering is known to be a proxy for suspended matter content in water. Herlevi (2002) found a correlation (R = 0.85) between the average total scattering (over AC–9 wavelengths) and the concentration of suspended matter for Finnish and Estonian lakes. In the case of our data, the averaged scattering coefficient did not give such a good correlation, but there was some correlation (R = 0.55) between the suspended matter concentration and the scattering coefficient at a wavelength of 715 nm. The corresponding linear regression formula is:

$$C_{SM} = 0.538 b(715) + 2.0683 . \qquad (29)$$

5.2 A Bio–optical model for Pakri Bay

Reflectance just above the surface is of interest for us as it is measured by remote sensing instruments. Equation (21) allows calculation of the subsurface irradiance reflectance, but to obtain the reflectance just above the surface Austin (1980) proposes a factor of 0.544 for the conversion of the irradiance reflectance just beneath the water surface to the reflectance just above the water surface, i.e. remote sensing reflectance is:

$$r\left(\lambda\right) = 0.544\left(0.629\mu_0 + 0.975\right)\frac{b_b\left(\lambda\right)}{a\left(\lambda\right)+b_b\left(\lambda\right)}. \qquad (30)$$

Knowledge of specific absorption and scattering coefficients of OAS is essential for bio-optical modelling. If to assume that there are three optically active components in water, the total absorption can be described by formula (24) and the total backscattering coefficient by formula (26).

The spectral shape and numerical values of specific absorption and backscattering coefficients of OAS may be different for different water types. For Pakri Bay the bio-optical model was developed with the specific absorption and backscattering coefficients of OAS calculated from experimental data.

Model parameters

In model (30) the absorption and scattering spectra of pure water, $a_w(\lambda)$ and $b_w(\lambda)$ were taken from Pope and Fry 1992.

The spectral absorption by CDOM can be expressed as a function of the absorption coefficient of dissolved material at a wavelength of 380 nm, $a_{CDOM}(380)$, and a slope factor, S_{CDOM}, by equation (22).

The $a_{CDOM}(\lambda)$ spectra were obtained from laboratory analyses of water samples from Pakri Bay. The slope values were estimated by fitting the exponential function to the measured λ and a_{CDOM} data. The average slope of –0.013 was calculated from 100 analysed spectra.

The chlorophyll-specific spectral absorption coefficient of phytoplankton was calculated using the power function (equation (23)) recommended by Bricaud et al. (1995)

The chlorophyll-specific spectral backscattering coefficient for phytoplankton was taken from Dekker (1993).

The particle-specific spectral absorption and backscattering coefficients for tripton can vary greatly in different water bodies. As for Pakri Bay no such data are available, equations (24) and (25) were used for calculating the particle–specific spectral absorption and backscattering:

$$a_t^*\left(\lambda\right) = \frac{a\left(\lambda\right) - a_{CDOM}\left(\lambda\right) - a_w\left(\lambda\right) - a_{ph}^*\left(\lambda\right)C_{chl}}{C_t}, \qquad (31)$$

$$b_t^*(\lambda) = \frac{b(\lambda) - b_w(\lambda) - b_{ph}^* C_{Chl}}{C_t}. \quad (32)$$

In equations (31) and (32), the spectra of total absorption and scattering coefficients measured by AC-9 are used. The $a_{CDOM}(\lambda)$ spectra were calculated from equation (22), $a_w(\lambda)$ and $b_w(\lambda)$ were taken from Pope and Fry (1997). The $a^*_{ph}(\lambda)$ was calculated according to equation (23) and $b^*_{ph}(\lambda)$was taken from Dekker 1993. The concentrations of chlorophyll *a* and suspended matter were determined from water samples. The concentration of tripton was calculated using the equation developed by Hoogenboom and Dekker (1997).

$C_t = C_{SM} - 0.07C_{chl}$ (33)

Obtained $a^*_t(\lambda)$ and $b^*_t(\lambda)$spectra averaged from 24 calculated spectra are shown on Figure 9.

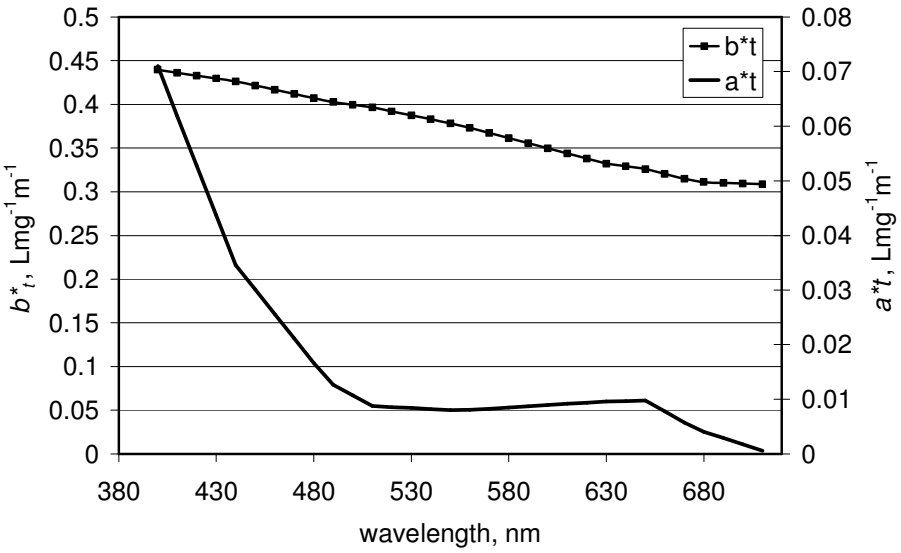

Figure 9. Particle-specific spectral absorption (a^*_t) and scattering (b^*_t) coefficients for the Pakri Bay bio-optical model.

In the model we need backscattering instead of scattering. To obtain particle-specific backscattering spectra the particle-specific scattering spectra were multiplied by backscattering probability value of 0.019. Herlevi (2002) showed that backscattering probability varies from 0.016 to 0.022 in Nordic waters. The obtained spectra of $a^*_t(\lambda)$ and $b_b{}^*_t(\lambda)$ were implemented in the model.

Application of the model

The spectra of the surface reflectance for different suspended matter concentrations were modelled using equation (30) and the model parameters described in the previous section. The concentration of chlorophyll *a* was kept fixed at 4 μg/L. For $a_{CDOM}(380)$ the value 1.84 m^{-1} was selected; it corresponds to the average measured value for Pakri Bay. S_{CDOM} was taken equal to –0.013 and μ_0 to 0.45. The values of C_t for different C_{SM} were calculated from equation (33). The modelled surface reflectance data with varying suspended matter concentration are shown in Figure 10. Figure 10 reveals that surface reflectance increases in the whole visible range of the spectrum with increasing suspended matter concentration in water. In the range of 620–670 nm, which corresponds to MODIS band 1 with spatial resolution of 250 m, the changes in the suspended matter concentrations up to ~30 mg/L have a grater effect on changes in surface reflectance than very high concentrations of suspended matter ~60 mg/L in our case (Figure 11).

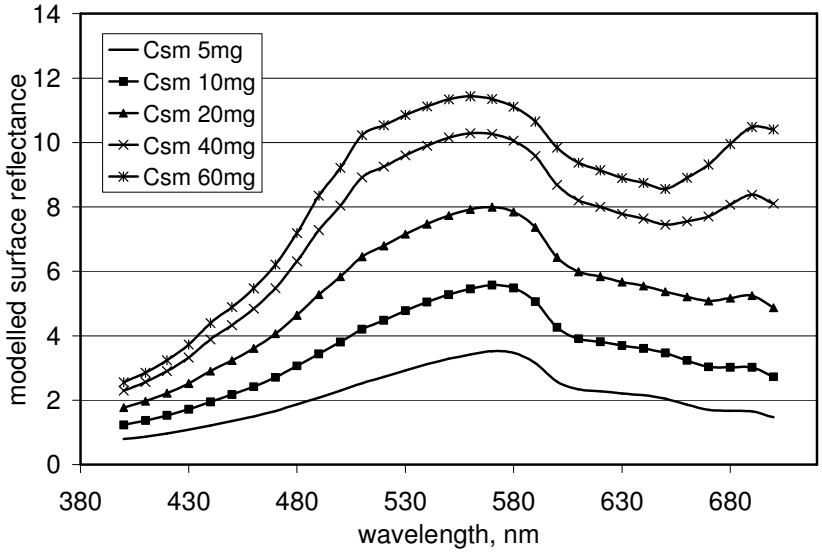

Figure 10. Modelled surface reflectance, with varying C_{SM} concentration.

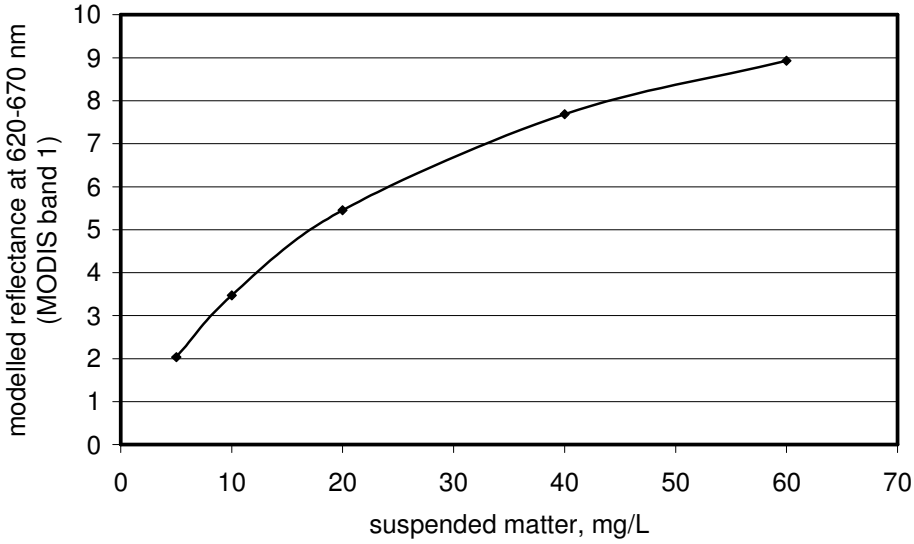

Figure 11. Modelled remote sensing reflectance vs. the suspended matter concentration.

The Modelled reflectance was also tested against the reflectance values measured by the MODIS instrument at band 1. The correlation coefficient of the modelled reflectance vs. the measured reflectance at band 1 was 0.72 (Figure 12). The analysis reveals that MODIS band 1 gives a reasonable result for the detection of the suspended matter distribution although it was designed for atmospheric use.

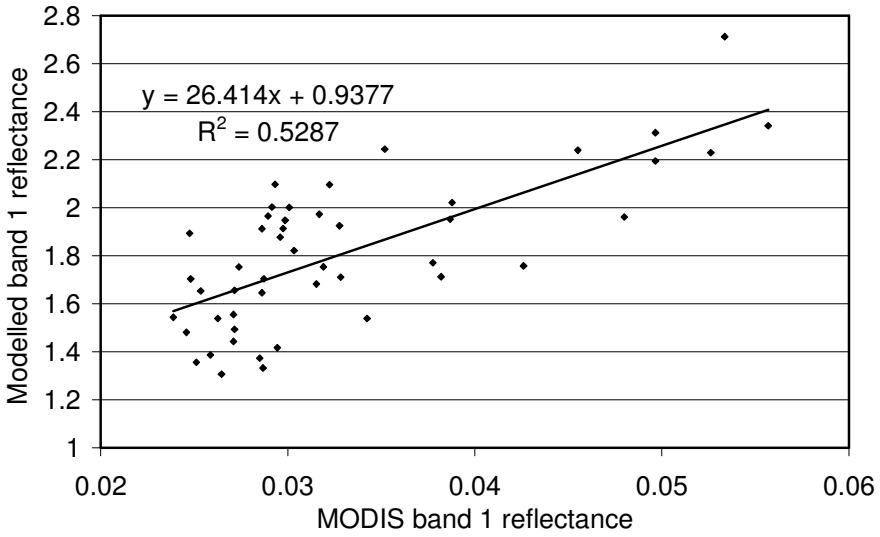

Figure 12. Modelled remote sensing reflectance vs. the reflectance measured at MODIS band 1.

5.3 Operational monitoring of suspended matter distribution during Paldiski South harbour dredging using MODIS imaginary and numerical modelling (Detailed treatment in Paper II)

The dredging activities in Pakri Bay were intensive in 2002–2003 when 1.500 000 million m^3 of material was removed from the shipping channel. The monitoring of suspended matter concentration during the harbour dredging in Pakri Bay was performed using a combination of remote sensing and numerical modelling together with *in situ* measurements.

The maps with suspended matter concentration were compiled using regression formula (27) described in the section methods.

To describe the distribution of suspended matter in Pakri Bay a numerical model was used in addition to remote sensing. The hydrodynamic model applied in this study is a finite difference model based on nonlinear shallow-water equations. The Lagrangian particle transport model was used for the calculation of the suspended particulate matter distribution. The particles were released to the water column from single or multiple point sources that depended on dredging activity. The number of discharged particles was proportional to the dredging amount and followed the time schedule of particular dredging. In the water column, the particles were transported by pre-calculated currents from the hydrodynamic model and dispersed randomly.

Time sequence of MODIS images and model distributions

The first image is from 25 April 2003, i.e. about 10 days from the beginning of dredging (Figure 13a). During the first period (15–22 April) daily amounts of dredged material were rather small (about 1000 m^3/day) because the bay was partly covered with ice. On the image, higher suspended matter concentrations (7.5–8.5 mg/L) are close to the Paldiski South Harbour and extend about 1 km offshore. The modelled suspended matter distribution shows a qualitatively similar pattern. Both the model results and the satellite image indicate that suspended matter is transported to the south along the coast. Comparison of the suspended matter concentration from the model results and the satellite image indicates that the concentrations up to 5 mg/L in the open part of Pakri Bay and Kurkse Strait may not represent suspended matter originating from a point source but may be caused by higher biological production in early spring.

The next image on 2 May shows that Pakri Bay is more strongly affected by dredging activity than earlier. A high suspended matter concentration can be identified along the entire eastern coast of the bay (Figure 13c). Moderate concentrations of suspended matter (6.5–7.5 mg/L) can be observed over the area between the Pakri Peninsula and Väike–Pakri Island, and in the southern bay. Low turbidity water is seen southward from Väike–Pakri Island with a tongue of low turbidity water that extends towards the Pakri Peninsula. The change in the suspended matter distribution pattern compared to the previous

image can be explained by moderate winds from southwest. These winds drive eastward and northward coastal currents in southern and eastern Pakri Bay, which transport a water mass with a high suspended matter concentration northward.

The next image on 11 May shows a decrease in the suspended matter concentration in general, except the area adjacent to the source (Figure 13e). The dredging amounts were considerably lower (about 2000 m^3/day on average) during a one week period before the image was obtained. The winds were weak to moderate and mainly from the southwest. The model suspended matter concentration shows a distribution pattern similar to the previous situation.

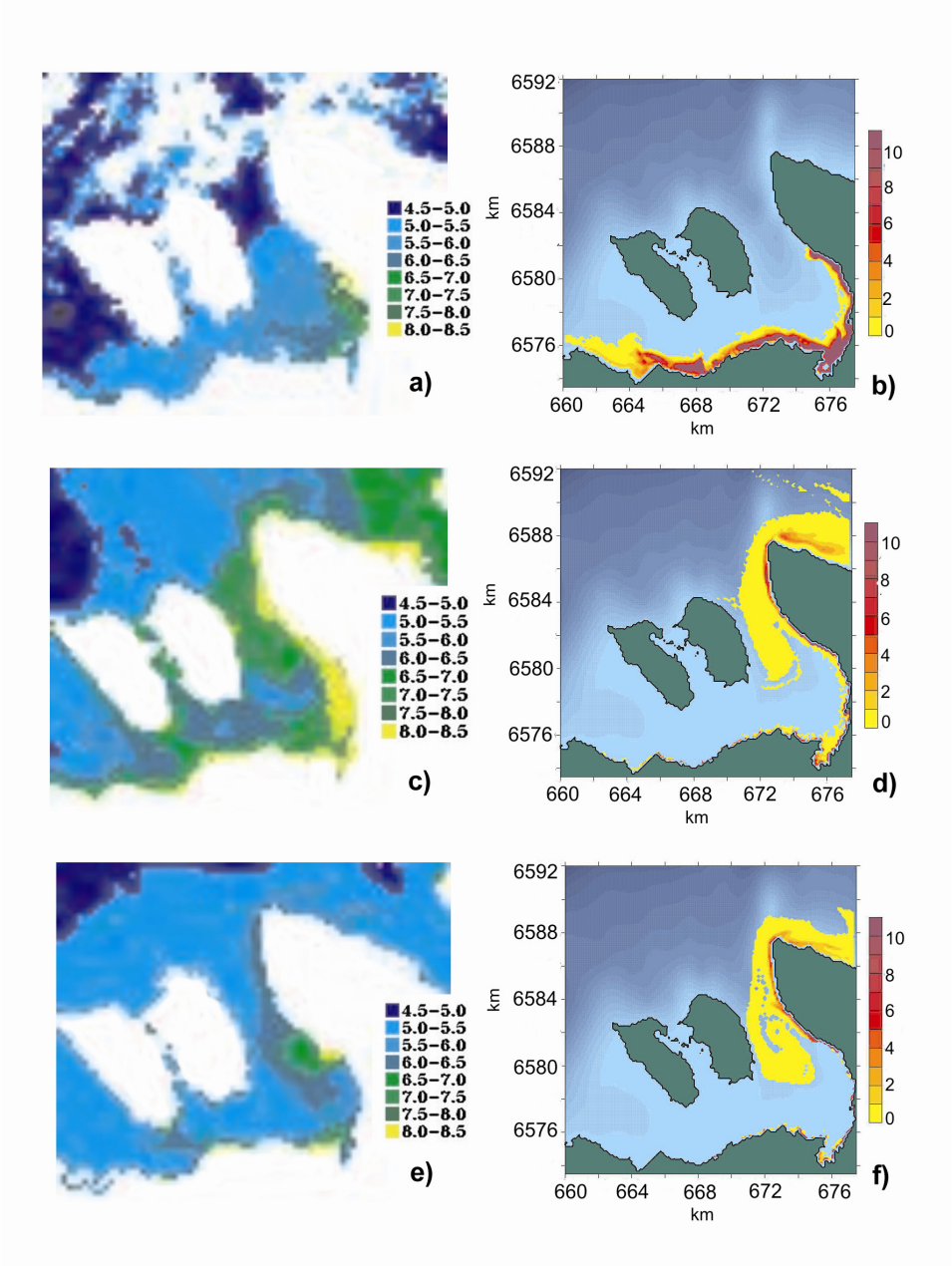

Figure 13. a) Distribution of suspended matter (SM) concentration (mg/L) from the MODIS image, 25 April 2003; b) Distribution of SM concentration (mg/L) from the model, 25 April 2003; c) Distribution of SM concentration (mg/L) from the MODIS image, 2 May 2003; d) Distribution of SM concentration (mg/L) from the model, 2 May 2003; e) Distribution of SM concentration (mg/L) from the MODIS image, 11 May 2003; f) Distribution of SM concentration (mg/L) from the model, 11 May 2003.

5.4 Physical properties of ice in the study region

Measurements of albedos (Detailed treatment in Paper IV)

Reflective properties of ice, i.e. ice albedos, are especially important from the point of view of remote sensing. The dependence of albedo on surface conditions according to our measurements is shown in Table 1. We can see a decrease in the values of snow albedo from very fresh snow to old and melting snow. Naturally, the values of A(snow) and A(snow removed) differ from each other, but the numerical values of these differences vary, depending on the reflective properties of ice cover and/or melting ice (as well of snow). In most cases A(snow removed) exceeds 0.5, which is systematically higher than A(ice). This is explained not only by the transparency properties causing a dark "colour" of some types of ice and/or melting ice (smaller scattering coefficients), but also by the fact that usually just below snow there is "snow ice" with rather high albedo. There can be also cases of scabrous ice, when we cannot totally remove all the snow (a small part of snow remains on the ice and increases its albedo).

Table 1. Variations of the surface albedo (obtained for the region 400-700 nm) of water bodies in wintertime from measurements in 2000–2003

Description of the surface	**Albedo**
Fresh snow	91–95
Snow	80–90
Old snow	67–73
Melting snow	63
Hoarfrost on the ice	51–58
Ice when snow is removed	37–70
Gray or dark gray ice	20–48
Melting ice	23–29
Remains of slush on the ice	22
Thin water layer on the ice	19

According to Ishikawa et al. (2003) the integral albedo measured at the Tvärminne Biological Station (Finland) was about 80 for snow, 30–35 for thick ice and 10–20% for thin (D < 10 cm) ice (step by step growth of the ice layer was observed). Note that the surface layer properties vary widely in snow and ice, in ways not so far quantified, and therefore quite different albedo values exist in the literature even for similar conditions.

Comparison of the data of Table 1 and Ishikava et al. (2003) show that in the Baltic Sea region thin (probably growing) ice and melting (covered with water or slush) ice give rather similar values of surface albedo.

Transmittance and light attenuation coefficient in ice (Detailed treatment in paper IV)

The measurements performed in winters 2000–2003 confirmed that transmittance was most strongly affected by the presence of snow cover. The ratio $T = E_d(D)/E_d(inc)$ as well as the corresponding thickness of snow and ice are shown in Figure 14. The values of T(snow removed) vary from 3.5 to 58%, being 2.5–14 times higher than T(snow+ice) (Figure 14a). Mean values of the light attenuation coefficient for ice cover calculated by equation (17) are presented in Figure 14b. We can see that $K_{d,i}$ for lakes is considerably lower than for Santala Bay (Figure 14b). This can be explained by the fact that the brackish ice contains brine pockets where phytoplankton may grow, which leads to an increase of the absorption of light in the ice. Also in brackish waters the ice captures more dissolved matter than in lakes (Paper III).

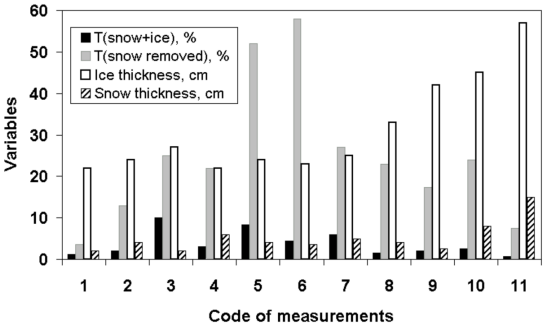

a)

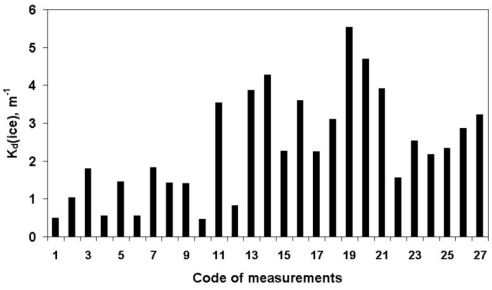

b)

Figure 14. a) Values of T(PAR) with and without snow cover and the corresponding thickness of snow and ice (only for lakes). b) . Vertically averaged light attenuation coefficient of ice cover in lakes (No 1-12) and in Santala Bay (No 13-27).

Impurities in lake and sea ice in the Baltic Sea region (Detailed treatment in Paper III)

The optical properties of ice impurities influence light attenuation in the ice and light penetration through the ice cover. Analysis of ice OAS in ice meltwater were performed during winters 2000–2003.

During freezing CDOM is partly separated from the growing ice into the underlying water. The separation factor in 20–50% in seawater but should be much less in very low salinity lake water (Weeks, 1988). A comparison of the amount of CDOM in ice meltwater and in the underlying water is shown in Figure 15a. The largest differences were obtained in eutrophic lakes (Võrtsjärv, Ülemiste) and dystrophic Nohipalu Mustjärv. The ratio of $c^*_f(380)$ between water and ice was more than 12, while in oligotrophic Lake Paukjärv this ratio was only 3 and in Santala Bay 4.

The concentrations of Chl *a* in lake ice are typically small (0–3 mg m^{-3}). The situation with sea ice varies, the lower surface being porous and green–coloured as algae grow in brine pockets. Here the maximum C_{chl} (13.5 mg m^{-3}) is in the lower layer of the ice.

The PAR band (400–700 nm)attenuation coefficient c^*(PAR) gives a good description of the amount of impurities. Figure 15b gives a general picture of the profiles of c^*(PAR) in ice and in the underlying water. In eutrophic lakes (Ülemiste, Võrtsjärv) the water beneath the ice is less transparent than the ice meltwater, but in clear lakes (Paukjärv) the opposite result was obtained. The atmospheric fallout on the ice of clear lakes caused a higher attenuation coefficient in the ice than in the water. In brackish waters the ice captures more dissolved matter than in lakes. In Santala Bay the ratio of $c^*_f(380)$ between the water and ice was 4. Also the ice meltwater there is more transparent than the water beneath the ice because brackish ice contains brine pockets where phytoplankton can grow.

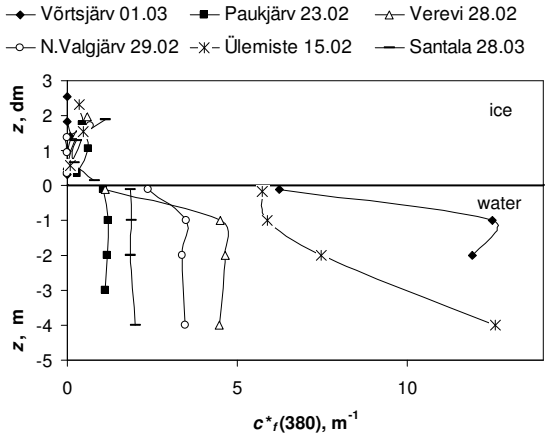

a)

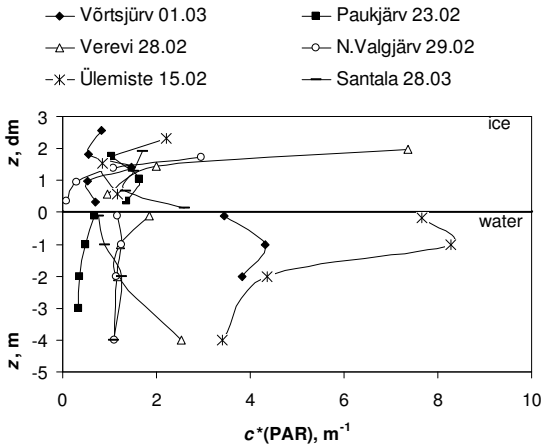

b)

Figure 15 a) Examples of vertical profiles of $c_f^*(380)$ in and under ice cover, measured in winter 2000. b) Examples of vertical profiles of c^*(PAR) in and under ice cover, measured in winter 2000. The zero point of the depth (z) scale is the lower border of the ice layer, the values of z in the ice are in decimetres, in the water z is negative and in meters.

5.6 Analysis of the ice cover extent in the Gulf of Riga in 2000–2005 using MODIS imaginary

Up to now no analysis of the ice cover extent based on detailed satellite data was available for the Gulf of Riga. Analysis of the ice cover extent in the Gulf of Riga using MODIS imaginary was performed for the period 2000–2005. The methods used in analysis are described in section 4.2.3. The number of cloud-free images that were suitable for ice cover analysis was different every winter. Table 2 shows the number of the MODIS images analysed per month in the winters of 2000/2001 to 2004/2005.

Table 2. Number of images per month analysed

year	Detsember	January	February	March	April
2000/2001	0	1	1	2	1
2001/2002	0	2	2	2	0
2002/2003	1	2	2	7	7
2003/2004	0	1	2	5	3
2004/2005	0	1	4	4	4

Four examples of ice cover maps from mid-March 2002–2005 are shown in Figure 16. Usually in mid March the maximum ice extent has been reached, and the ice starts to melt.

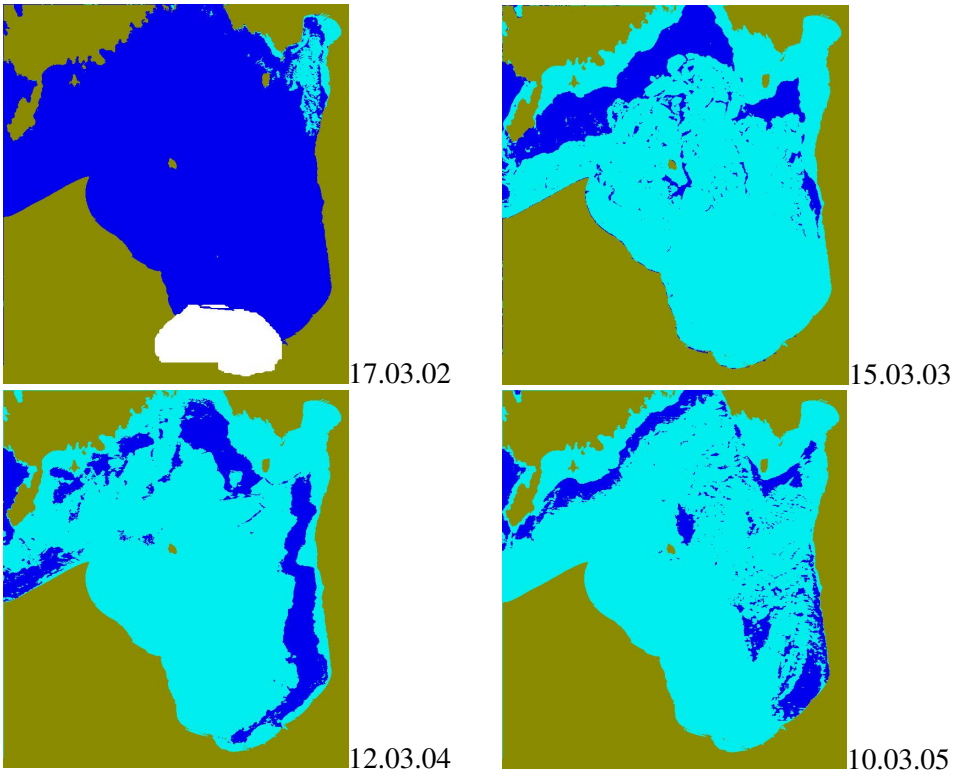

Figure 16. Examples of ice coverage maps for Gulf of Riga for mid-March 2002–2005. Dark blue represents the open water, light blue ice and yellow is land.

The calculated ice extent in square kilometres during winters 2000–2005 is shown in Figure 17. Analysis revealed that the duration and the extent of ice cover differed greatly during these years. Winters 2000/2001 and 2001/2002 were mild, the maximal ice extent in the Gulf of Riga was less than 2000 km^2 and the ice season lasted only from January till the end of March. Winter 2002/2003 was quite severe. The ice cover formed already in November and by the end of December the Gulf of Riga was fully ice covered (ice extent was up to 16 000 km^2) and stayed that way until the middle of March. During the second decade of March the ice stared to melt slowly but still some ice was distinguished from MODIS images until the beginning of May. In winter 2003/2004 ice started to form at the beginning of January and slowly continued to grow for a month and by the mid-February the ice cover was up to 14 000 km^2, which was the maximum during that winter. The ice extent stayed at its maximum until mid-March and then rapidly started to melt. By the middle of April the Gulf of Riga was ice free. In winter 2004/2005 the ice started to form in the Gulf of Riga at the end of January. The ice cover reached its maximum in

mid-March and the Gulf of Riga stayed totally ice covered (ice extent up to 16 000 km^2) until the end of March, then within two weeks the ice cover melted.

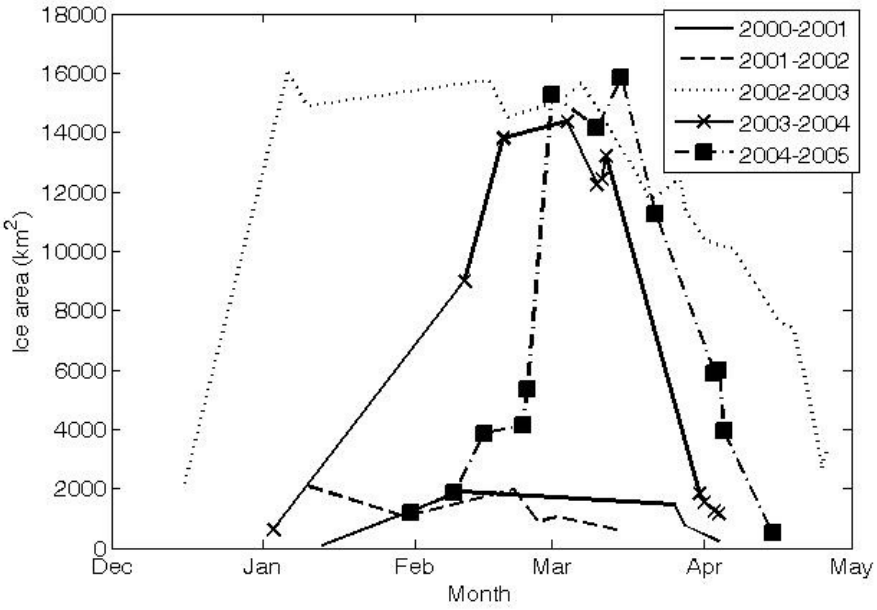

Figure 17. Ice extent (km^2) in the Gulf of Riga during winters 2000–2006.

6. Conclusions

The analysis of inherent optical properties of seawater showed that light attenuation and absorption spectra were rather similar in different locations of the northwestern Estonian coastal sea. In the light attenuation, scattering dominated over absorption.

Relationships between inherent optical properties and concentrations of optically active substances in the seawater were examined. Our results showed that there was a strong correlation between the CDOM content in water and the absorption at 412 nm. The correlation between the absorption at 676 and chlorophyll *a* content in water was insignificant. The suspended matter concentration correlated best with the scattering coefficient at 715 nm.

A Bio-optical model for Pakri Bay that enables to calculate the surface reflectance was developed. The model was used for the evaluation of the sensitivity of MODIS band 1 (620–670 nm) for calculating the suspended matter concentration in surface water. Analysis revealed that the sensitivity of MODIS band 1 is higher for lower (up to ~30 mg/L) concentrations of suspended matter than for higher concentrations (over ~30 mg/L).

The MODIS band 1 data (250 m spatial resolution) were applied for analysing the suspended matter concentration during an extensive harbour dredging in Pakri Bay. This case study showed that MODIS images can be used for monitoring the suspended matter concentrations in the coastal sea, including a relatively small bay. Even though the bio-optical model was developed for Pakri Bay, the linear regression between remote sensing reflectance and suspended matter concentrations determined from water samples gave reasonable results that allow converting reflectance values into suspended matter concentrations.

Analysis of wintertime data showed that ice surface albedo of the water bodies varies in great limits, from about 95% for fresh snow to 19–22% for slush or a thin water layer on the ice. Light transmittance is about 2.5–14 times higher for snow free ice than for snow coverd ice. The vertically averaged diffuse attenuation coefficient in ice is considerably lower for lake ice than coastal sea ice, e.g. Santala Bay.

Application of MODIS band 1 data (250 m spatial resolution) for the calculation of the ice cover extent in the Gulf of Riga during winters 2000–2005 reviled a significant variation of ice cover extent from year to year. In mild winters, i.e. 2000/2001 and 2001/2002, the maximum ice extent was up to 2000 m^2. In moderate and severe winters, i.e. 2002/2003 2003/2004 and 2004/2005, ice covered the entire Gulf of Riga, but the date and duration of full coverage were different. Additionally, MODIS data can be used for distinguishing snow covered fast ice from new and melting ice.

Acknowledgements

I wish to express my thanks to Dr Helgi Arst and the Marine Optics Group at the University of Tartu where I started to work with the problems of marine optics. I am also grateful to my supervisor and colleagues from the Marine Systems Institute at TUT for helping me in this work.

References

Ackerman, S.A., Strabala, K.I., Menzel, P.W.P., Frey, R.A.., Moeller, C.C, Gumley, L.E. 1998. Discriminating clear sky from clouds with MODIS. J. Geophys. Res., 103, 32141–32157.

Ahn,Y. H. 1990. Optical properties of biogenous and mineral particles present in the ocean. Application: inversion of reflectance. Thesis, Paris-VI University.

Allison, I., Brandt, R.E., Warren, S.G. 1993. East antarcic sea ice: albedo, thickness distribution and snow cover. J. Geophys. Res., 98, 12417–12429.

Austin, R.W. 1980. Gulf of Mexico, ocean color surface truth measurements. Boundary-layer Meteorology, 18, 269–285.

Bricaud, A., Morel, A., Prieur, L. 1983. Optical efficiency factors of some phytoplankters . Limnol. Oceanogr., 28, 816–832.

Bricaud, A., Babin, M., Morel, A., Claustre, H. 1995.Variability in the chlorophyll-specific absorption coefficients of natural phytoplankton: analysis and parametrisation. J. Geophys. Res., 100, 13321–13332.

Bricaud, A., Stramski, D. 1990. Spectral absorption coefficients of living phytoplankton and non-algal biogenous matter: a comparison between the Peru upwelling area and Sargasso Sea. Limnol. Oceanogr., 35, 562–582.

Claustre, H.. Fell F., Oubelkheir, K., Prieur, L. 2000. Continues monitoring of surface optical properties across a geostrophic front: Biogeochemical inferences. Limnol. Oceanogr. 45, 2. 309–321

Dekker, A.G. 1993. Detection of optical water quality parameters for eutrophic waters by high resolution remote sensing. PhD thesis. Free University, Amsterdam.

Gordon, H.R., Brown, O.B., Jacobs, M.M. 1975. Computed relationships between the inherent and apparent optical properties of flat homogenous ocean. Appl. Optics, 14, 417–427.

Grenfell, T.C. 1983. A theoretical model of the optical properties of sea ice in the visible and near infrared. J. Geophys. Res., 88, 9723–9835

Grenfell, T.C. 1991. Radiative transfer model for sea ice with vertical structure variations. J. Geophys. Res., 96, 16991–17001.

Grenfell, T.C, Maykut, G.A. 1977. The optical properties of ice and snow in the Arctic Basin. J. Glaciol., 18, 445–463.

Hall, D.K., Riggs, G., Salomonson, N.E., DiGirolamo, N.E., Bayr, K.J. 2002. MODIS snow-cover products. Remote Sensing Environ., 83, 181–194.

Herlevi, A. 2002. Inherent and apparent optical properties in relation to water quality in Nordic waters. Academic dissertation in Geophysics. University of Helsinki. Finland.

Hoogenboom, J., Dekker, A.G. 1997. Simulation of the medium-resolution imaging spectrometer (MERIS) performance for detecting chlorophyll-*a* over turbid inland waters. SPIE Proc., 2963, 440–447.

Højerslev, N. K. 1980. On the origin of yellow substance in the marine environment. Oceanogr. Rep., Univ. Copenhagen, Inst. Phys. 42.

Højerslev, N.K., Aas, E. 2001. Spectral light absorption by yellow substance in the Kattegat–Skagerrak area. Oceanologia, 43, 39–60.

Hu, C., Chena, Z., Claytonb, T.D., Swarzenskib, P., Brockb, J.C., Muller-Karger, F.E. 2004. Assessment of estuarine water-quality indicators using MODIS medium-resolution bands: Initial results from Tampa Bay, FL. Remote Sensing Environ., 93, 423–441.

Ishikava, N., Takizawa, A., Kawamura, T., Shirasawa, K., Leppäranta, M. 2003. Changes of the radiation property with sea ice growth in Saroma Lagoon and the Baltic Sea. In: Rep. Ser. Geophys., No 46, University of Helsinki, Hokkaido University, Helsinki, 147–160.

Jerlov, N.G. 1968. Optical Oceanography. Elsevier, Amsterdam.

Kirk, J.T.O. 1981. Estimation of the scattering coefficient of natural waters using underwater irradiance measurements. Australian J. Mar. Freshwater Res., 32, 533–539.

Kirk, J. T. O. 1984. Volume scattering function, average cosines, and the underwater light field. Limnol. Oceanogr., 29, 350–356.

Kirk, J.T.O. 1984. Dependence of relationship between inherent and apparent optical properties of water on solar altitude. Limnol. Oceanogr., 29, 350–356.

Kirk, J. T. O. 1994. Light and Photosynthesis in Acuatic Ecosystem, University Press, Cambridge.

Kowalczuk, P. 1999. Seasonal variability of yellow substance absorption in the surface layer of the Baltic Sea. J. Geophys. Res., 104, 30047–30058.

Kutser, T. 1997. Estimation of water quality in turbid inland and coastal waters by passive optical remote sensing. PhD Thesis. University of Tartu, Estonia.

Lindfors, A., Rasmus, K. 2000. Flow through system for distinguished dynamic features in the Baltic Sea. Geophysica, 36, 203–214.

Maykut, G.A., Grenfell, T.,C. 1975. The spectral distribution of light beneath first-year sea ice in the Arctic Ocean. Limnol. Oceanogr., 20, 554–563.

Maykut, G.A., Light, B. 1995. Refractive index measurements in freezing sea ice and sodium chloride brines. Appl. Optics, 34, 950–961.

Maykut, G.A., Petrovich, D.K. 1987. On the role of shortwave radiation in the summer decay of sea ice cover. J. Geophys. Res., 92, 7032–7044.

Maykut, G.A., Untersteiner, N. 1971. Some results from a time dependent thermodynamic model of sea ice. J. Geophys. Res., 76, 1550–1575.

Miller, R.L., McKee, B.A. 2004. Using MODIS Terra 250 m imagery to map concentrations of total suspended matter in coastal waters. Remote Sensing Environ., 93, 295–266.

McKee, D., Cannigham, A., Slater, J., Jones, K.J., Griffits, C.R. 2003. Inherent and apparent optical properties in coastal waters: a study of the Clyde Sea in early summer. Estaurine, Coastal Shelf Sci., 56, 369–376.

Mobley, C., D. 1994. Light and Water: Radiative transfer in natural waters. Academic Press, San Diego.

Pavelson, J., Kononen, K., Laanemets, J. 1999. Chlorophyll distribution patchiness caused by hydrodynamical processes: a case study in the Baltic Sea. J. Mar. Sci., 56, 87–99.

Perovich, D. K. 1993. A theoretical model of ultraviolet light transmission through Antarctic sea ice. J. Geophys. Res., 98, 22579–22587.

Perovich, D. K. 1994. The optical properties of sea ice. In: Physics of Ice Covered Seas. Lecture notes from a summer school in Savonlinna, Finland 6–17 June, 1994, 195–230.

Pope, R.M., Fry, E.S. 1997. Absorption spectrum (380–700 nm) of pure water. II. Integrating cavity measurements. Appl. Optics, 36, 8710–8723.

Prieur, L. 1976. Transfer radiatif dans les eaux de mer, D.Sc dissertation. Paris: Université Pierre et Marie Curie.

Reinart, A. 2000. Underwater light field characteristics in different types of Estonian and Finnish lakes. PhD Thesis. University of Tartu, Estonia.

Riggs, A.G., Hall, K.D., Ackerman, A.S. 1999. Sea ice extent and classification mapping with the Moderate Resolution Imaging Spectroradiometer airborne simulator. Remote Sensing Environ., 68, 152–163.

Smith, R.C., Baker, K.S. 1981. Optical properties of the clearest natural waters (200–800nm) Appl. Optics, 20, 177–184.

SooHoo, T.B., Palmisano, S.T., Kottimeier, M.P., Lizotte, S.L., Sullivan, C.W. 1987. Spectral light absorption and quantum yield of photosynthesis in sea ice microalge and a bloom of *Phaeocystis pouchettii* from McMurdo Sound, Antarctica. Mar. Ecol., 33, 175–189.

Suursaar, Ü., Astok, V., Kullas, T., Nõmm, A., Otsmann, M. 1995. Currents in the Suur Straight and their role in the nutrient exchange between the Gulf of Riga and the Baltic Proper. Proc. Estonian Acad. Sci. Ecol. 5, 103–123.

Tyler, J.E., Smith, R.C. 1970. Measurements of Spectral Radiance Underwater. Gordon and Breach, New York.

Weeks, W.F. 1998. Growth conditions and the structure of sea ice. In Leppäranta M. (ed.). Physics of Ice-covered Seas. Department of Geophysics, University of Helsinki. 5–105.

Weller, G. 1972. Radiation flux investigations. AIDJEX Bull., 14, 28–30.

Abstract

The main aim of the present study was to evaluate the possibilities of using remote sensing for the monitoring of suspended matter and ice in seawater. Data from a spectrometer MODIS installed at NASA satellites Terra and Aqua were used. Two methods were applied for the interpretation of remote sensing data: a bio-optical model and an empirical regression model.

First, the suitability of optical characteristics (absorption and scattering coefficient) for the estimation of concentrations of optically active substances (suspended matter, chlorophyll *a* and coloured dissolved organic matter) was studied using flow-through measurement data from coastal waters of north-western Estonia. Our results showed that there was a strong correlation between the CDOM content in seawater and the absorption at 412 nm. The correlation between the absorption at 676 nm and chlorophyll *a* content was insignificant. The suspended matter concentration correlated best with the scattering coefficient at 715 nm.

A bio-optical model for Pakri Bay that enables to calculate the surface reflectance was developed. The model was used for the evaluation of the sensitivity of MODIS band 1 (620–670 nm) for the calculation of suspended matter concentration in surface water. The results of the analysis revealed that the sensitivity of MODIS band 1 is higher for lower (up to ~30 mg/L) concentrations of suspended matter than for higher concentrations (over ~30 mg/L).

The MODIS band 1 data (250 m spatial resolution) were applied for the analysis of suspended matter concentration during an extensive harbour dredging in Pakri Bay. The linear regression model between remote sensing reflectance and suspended matter concentrations determined from water samples was used for converting reflectance values into suspended matter concentrations. The analysis showed that the east coast of Pakri Bay was the most affected by high concentration of suspended matter. There were two prevalent distributions of suspended matter depending on winds: in the case of the northern winds the suspended matter was transported to the south of Pakri Bay and in the case of the southern winds the suspended matter was transported out of the bay

Application of MODIS band 1 data (250 m spatial resolution) for the calculation of the ice area in the Gulf of Riga during winters 2000–2005 revealed a significant variation of ice cover area from year to year. In mild winters, i.e. 2000/2001 and 2001/2002, the maximum ice area was up to 2000 m^2. In moderate and severe winters, i.e. 2002/2003 2003/2004 and 2004/2005, ice covered the entire Gulf of Riga, but the initial date and duration of the formation of full ice coverage were different. Additionally, MODIS data can be used for separating snow covered fast ice and new and melting ice.

Kokkuvõte

Käesoleva uurimustöö peamiseks eesmärgiks oli hinnata satelliitkaugseire rakendusvõimalusi heljumi ja jää seireks meres. Uurimustöös kasutati satelliitseiresüsteemi MODIS andmeid, mis on paigaldatud NASA satelliitidele Terra ja Aqua. Satelliitandmete sobivuse väljaselgitamiseks kasutati kaht meetodit: koostati bio-optiline mudel ja kasutati ka empiirilist seost.

Kõigepealt hinnati optiliste karakteristikute (neeldumis- ja hajumiskoefitsient) sobivus optiliselt aktiivsete ainete (heljum, klorofüll a, lahustunud orgaaniline aine) kontsentratsioonide määramiseks kasutades läbivoolusüsteemi mõõtmisi Loode-Eesti rannikumeres. Pinnamõõtmised näitasid, et neeldumiskoefitsient lainepikkusel 412 nm sobib hästi lahustunud orgaanilise aine jaotuse hindamiseks. Klorofüll *a* kontsentratsiooni hindamiseks analüüsitud andmete korral olulist seost ei leitud. Heljumi hulga hindamiseks sobis enim hajumiskoefitsent lainepikkusel 715 nm.

Pakri lahe jaoks koostati bio-optiline mudel, mille abil hinnati satelliidi poolt mõõdetud heleduse muutlikust muutuva heljumi kontsentratsiooni korral Pakri lahes. Mudelarvutused MODIS seiresüsteemi kanal 1 (620–670 nm) sobivuse kohta heljumi kontsentratsiooni hindamiseks Pakri lahes näitasid, et suure heljumi kontsentratsiooni korral (enam kui 30 mg/L) kanal 1 tundlikkus väheneb.

Jäävabal perioodil kasutati MODIS kanal 1 andmeid heljumi kontsentratsiooni ja ruumilise jaotuse kaardistamiseks Pakri lahes toimunud süvendustööde ajal rakendades MODIS sensori poolt mõõdetud heleduse ja mõõdetud heljumi kontsentratsioonide vahel leitud lineaarset regressiioonseost. Analüüsi tulemused näitasid, et Pakri lahes oli süvendustöödest tingitud kõrgest heljumi kontsentratsioonist enam mõjutatud Pakti lahe idarannik ning vastavalt tuuleoludele oli lahes valdavaks kaht tüüpi heljumi jaotus: põhjakaarte tuule korral liikus heljum Pakri lahe pärasse ja lõunakaarte tuule korral liikus heljum Pakri lahe suudmealale ja lahest välja.

Talvistes tingimustes kasutati MODIS seiresüsteemi andmeid Riia lahe jääkaartide koostamiseks aastatel 2000/2005. Koostatud detailsete jääkaartide põhjal arvutatud jää pindala Riia lahes on pehmetel talvedel (2000/2001 ja 2001/2002) kuni 2000 km^2, keskmistel talvedel (2003/2004 ja 2004/2005) ning karmil talvel (2002/2003) oli maksimaalne jää pindala 16000 km^2, mis näitab, et kogu Riia laht oli täielikult jääga kaetud. Samal ajal maksimaalse jää pindala ajaline kestvus oli erinev kõikidel aastatel. MODIS'e andmed võimaldavad eristada lumega kaetud kinnisjääd noorest tekkivast jääst ja sulavast jääst.